Using solar-sail induced dynamics to increase the warning time for solar storms heading towards earth

Bakx, N.K.M.; Heiligers, M.J.

Publication date
2021

Document Version
Final published version

Published in
Proceedings of the Aerospace Europe Conference 2021

AerospaceEurope Conference2021
WARSAW, POLAND | 23 -26 NOVEMBER 2021
CEAS Council of European Aerospace Societies

USING SOLAR-SAIL INDUCED DYNAMICS TO INCREASE THE WARNING TIME FOR SOLAR STORMS HEADING TOWARDS EARTH

N. K. M. Bakx[1] & M. J. Heiligers[1]

[1]Delft University of Technology, Faculty of Aerospace Engineering, Kluyverweg 1, 2629 HS Delft, The Netherlands

Abstract

Coronal Mass Ejections (CMEs), commonly referred to as solar storms, that are on an Earth-intersecting trajectory, may lead to the breakdown of power grid transformers, the malfunctioning of Earth-orbiting spacecraft, and disruptions in navigation and communication systems, among many other effects. The financial impact of a solar storm is predicted to be in the order of trillions of euros and the probability of such an event occurring within the next decade is 12%. With society relying ever-more on technology, the impact of a solar storm is ever-increasing. It is therefore essential that operators of vital infrastructure are notified of an approaching storm in a timely manner such that they can take adequate measures to mitigate the impact. This paper investigates the use of solar-sail technology to increase the warning time for CMEs heading towards Earth. The warning time is proportional to the distance from the Earth to the spacecraft detecting the CME: a current warning time of 30 to 60 minutes is achieved by satellites at or near the Sun-Earth L_1 point. By considering the actual shape of a CME, the continuous solar-sail acceleration from the solar sail can be used to find a periodic trajectory that travels further upstream of the CME-axis, thereby increasing the warning time with respect to current missions. Finding a periodic solar-sail trajectory can be regarded as an optimal control problem, which requires a near-feasible initial-guess trajectory. The latter is found by generating heteroclinic connections between artificial equilibrium points in the vicinity of the sub-L_1 and sub-L_5 point through the use of a genetic algorithm. The optimal control problem is solved with a direct pseudospectral method, resulting in four representative trajectories, each having specific (dis)advantages. Ultimately, with near-term solar-sail technology (a lightness number of 0.05), the most optimal trajectory increases the average and maximum warning time by a factor 20 and 30 with respect to current missions at L_1, respectively, with a 90% probability that the spacecraft detects the CME. Finally, the paper investigated a set of sensitivity analyses (non-ideal sail properties and change in lightness number) to successfully prove the robustness of the methodology and the effect of assumptions made.

Keywords: Solar storm, Solar sail, Trajectory optimisation, Pseudospectral collocation

1. Introduction

Space weather caused by the Sun can have serious consequences on Earth and its society [1]. Explosive releases of plasma, also called Coronal Mass Ejections (CMEs) or solar storms, that are headed towards Earth interfere with Earth's magnetic field and, among others, expose humans to a larger dose of radiation, disrupt communication and navigation systems, and induce an electric current in wires. This electric current can, for example, cause power grids to break down and cause Earth-orbiting spacecraft to malfunction [2]. The economic impact of such a solar storm is predicted to be in the order of trillions of euros and the chance of an occurrence of a strong solar storm is estimated to be 12% in a decade, making it a realistic occurrence in a lifetime [3, 4, 5]. Combined with the fact that there is an increasing dependency in society on technology, it is essential that people receive a timely warning of an approaching solar storm so that adequate measures can be taken to mitigate the impact. It is estimated that two to three days are required to prepare for disruption [6].

Currently, solar storms are detected and warned for by spacecraft orbiting the Sun-Earth L_1 point such as SOHO (ESA/NASA, 1996), ACE (NASA, 1997), WIND (NASA, 2004), and DSCOVR (NOAA/NASA, 2015) [7]. Due to the difference in time between the solar-storm arrival and the spacecraft warning signal reception at Earth, a solar-storm warning time of 30 to 60 minutes can typically be achieved [8]. Consequently, the solar-storm warning time can be increased if the CME is detected further upstream of its propagation path, i.e., closer to the Sun. A solar sail can be utilised to this end by exploiting the continuous solar-sail acceleration to shift the Sun-Earth L_1 point sunward, called the SL_1 (sub-L_1) point [8]. This continuous acceleration results from the reflection of solar photons off a highly reflective membrane, which is, as opposed to conventional methods that depend on expelling mass, only limited by the lifetime of the sail [8]. In addition to a sunwards shift of the L_1 point, solar-sail assisted manifolds of the SL_1 point may be able to substantially increase the solar-storm warning time by allowing the spacecraft to travel even further upstream of the CME propagation path [9].

The first practical ideas of using a solar sail date back to 1920, when Tsiolkovsky and Tsander discussed using "tremendous mirrors of very thin sheets" [8]. In 2010, solar sailing became a reality by the successful launch of JAXA's IKAROS mission, followed by NASA's NanoSail-D2 mission in the same year [10, 11]. These missions were later followed by LightSail-1 (2015) and -2 (2019) from The Planetary Society [12]. Planned missions are NASA's NEA Scout (2021), NASA's ACS3 (2022), and JAXA's OKEANOS (2026) [13, 14, 15].

There has not yet been an actual solar-sail mission dedicated to solar-storm detection. However, theoretical studies show promising results of an increase in solar-storm warning time using the concept of solar sailing. In particular, NASA's Sunjammer and the Geostorm missions were designed to be stationed in an orbit about the Sun-Earth SL_1 point, allowing for an increase in solar-storm warning time of almost a factor two compared to traditional missions at the Sun-Earth L_1 point [7, 8]. Another concept exploits the unstable sunward manifold of a solar-sail halo orbit around the Sun-Earth SL_1 point to travel upstream of a CME by constantly replenishing the manifold with small high area-to-mass ratio spacecraft, also called SpaceChips [16, 17]. As there will always be a spacecraft upstream of the CME path, an increase in solar-storm warning time of approximately a factor nine can be achieved compared to mission designs that remain relatively close to the SL_1 point [16]. The main downside of this mission concept is that the lifetime of the mission is restricted by the number of SpaceChips. In addition, note that all these studies assumed that a CME propagates along the Sun-Earth line. A study that considered the actual shape of a CME while it propagates through interplanetary space is Ref. [9], which proposed the use of homo- and heteroclinic connections between Artificial Equilibrium Points (AEPs) in the vicinity of the Sun-Earth SL_1 point to increase the solar-storm warning time [18]. This concept resulted in an average increase in solar-storm warning time of approximately a factor 15 compared to current missions at the L_1 point, which is a substantially larger increase than what is achieved by the Sunjammer and Geostorm mission concepts [9]. Furthermore, as opposed to the work in Ref. [16, 17], the trajectory is periodic, meaning that a constant replenishment of spacecraft is not required.

The results of Ref. [9] were promising, but only considered trajectories in the vicinity of the SL_1 point, thereby potentially restricting the search space too much. Consequently, this study will focus on finding solar-sail periodic trajectories in the vicinity of both the SL_1 and SL_5 points. These trajectories are defined as an optimal control problem and will be solved using an open-source direct pseudospectral algorithm: PSOPT [19]. The objective of the optimal control problem defined in this work consists of three performance metrices: the average increase in warning time along the trajectory, the average distance to the CME-axis (which is correlated to the probability of CME-detection), and the maximum increase in warning time at any point along the trajectory. Note that the algorithm requires an (almost-)feasible initial guess trajectory for initiation, which, comprises heteroclinic connections between AEPs in the vicinity of the SL_1 and SL_5 points.

2. Dynamics

This section presents the models that will be utilised in the remainder of the paper. In particular, the dynamical model, the solar-sail model, and the CME-model are discussed. Moreover, this section will present the effects of the addition of a solar-sail acceleration to the classical (i.e., unperturbed)

dynamics and its potential usefulness with regards to solar-storm detection. Each section presents a model or insight that acts as a building block for the remainder of the paper.

2.1 Dynamical Model

Following the approach taken in previous studies [9, 7], the Sun-Earth Circular Restricted Three-Body Problem (CRTBP) is adopted as the dynamical model. In particular, a two-dimensional formulation, referred to as the planar CRTBP (PCRTBP), is employed as a CME that is headed towards Earth shows a clear correlation between its path and the ecliptic plane (more information on this is given in Section 2.3) [18]. As a result, limiting this study to the motion of a solar-sail spacecraft in the ecliptic plane is justified. The PCRTBP describes the two-dimensional motion of an infinitesimally small mass (spacecraft), m, under the gravitational influence of the masses of the two primaries: the Sun's mass, m_1, and the Earth's mass, m_2. The gravitational influence of the spacecraft on the two primaries is neglected. In addition, it is assumed that the Sun and the Earth move in circular orbits about the barycenter of the system. A graphical overview of the dimensionless Sun-Earth PCRTBP can be seen in Fig. 1.

The reference frame that is used to express the equations of motion is a synodic reference frame, $C(x,y)$, with the origin C at the barycenter, the x-axis is oriented along the line from the Sun to the Earth, and the y-axis lies in the ecliptic plane perpendicular to the x-axis. The frame rotates around the z-axis, which is oriented perpendicular to the ecliptic plane, at a constant angular velocity of $\vec{\omega} = \omega\hat{z}$ and is equal to the angular velocity of the Earth around the Sun.

The PCRTBP can be written in a dimensionless manner by defining the units of mass, length, and time. The unit of mass is set equal to the sum of the masses of the Sun and the Earth and the unit of length as the distance between the Sun and the Earth. The dimensionless mass of m_2 is defined as [8]

$$\mu = \frac{m_2}{m_1 + m_2} \tag{1}$$

and can subsequently be used to define the dimensionless mass of the Sun: $1-\mu$. The parameter μ is equal to 3.0404x10^{-6} in the Sun-Earth system. The unit of time is set to $1/\omega$, with $\omega = 1$, such that one year becomes 2π in dimensionless time units.

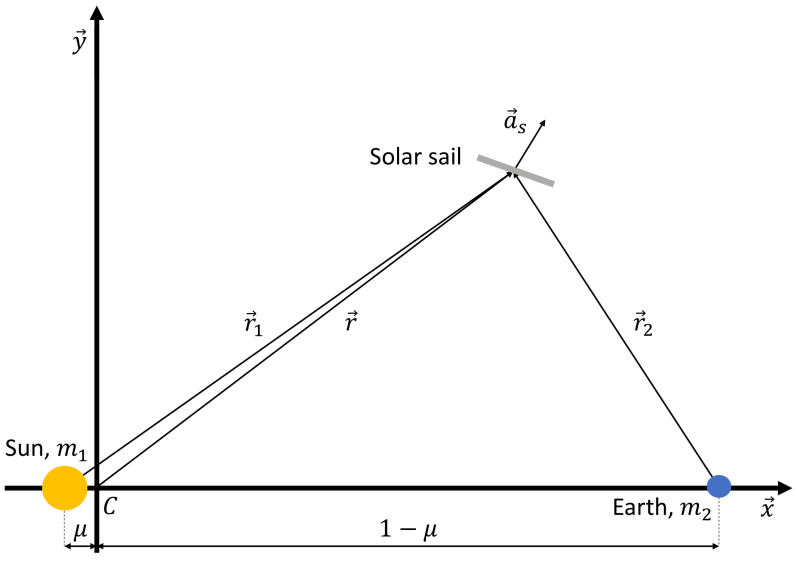

Figure 1 – Graphical overview of a solar sail in the Sun-Earth planar circular restricted three-body problem.

In the synodic reference frame $C(x,y)$ the motion of the spacecraft is described by [8]

$$\ddot{\vec{r}} = \vec{a}_s - \nabla U - 2\vec{\omega} \times \dot{\vec{r}} \tag{2}$$

where $\vec{r} = [x \quad y]^T$, $\vec{a}_s$ is the solar-sail acceleration, and U is the effective potential, which is equal to [8]

$$U = -\frac{x^2+y^2}{2} - \left(\frac{1-\mu}{r_1} + \frac{\mu}{r_2}\right) \tag{3}$$

where the position vectors from the Sun and the Earth to the spacecraft are denoted as $\vec{r}_1$ and $\vec{r}_2$, respectively, $r_1 = |\vec{r}_1|$, $r_2 = |\vec{r}_2|$, $\vec{r}_1 = [x+\mu \quad y]^T$, and $\vec{r}_2 = [x-(1-\mu) \quad y]^T$.

2.2 Solar-sail Model

In this study, for the definition of the solar-sail acceleration both an ideal and an optical solar-sail model are adopted. Both models assume that the sail is perfectly flat. However, while the ideal model assumes pure specular reflection of the incident photons, the optical sail model accounts for absorption, diffuse reflection, and thermal emission [8]. The ideal model is more insightful, while the optical solar-sail model is more realistic than an ideal model and therefore more relevant [8]. Therefore, at first, the ideal solar-sail model is used which is later replaced by the optical model in the sensitivity analysis (Section 3.4).

The solar-sail acceleration can be expressed in a term that is tangent to the solar sail, $a_t\hat{\vec{t}}$ and a component normal to the sail, $a_n\hat{\vec{n}}$ as

$$\vec{a}_s = a_s\hat{\vec{m}} = a_t\hat{\vec{t}} + a_n\hat{\vec{n}} \tag{4}$$

where $\hat{\vec{m}}$ is a unit vector in the direction of the total solar-sail acceleration. A graphical representation

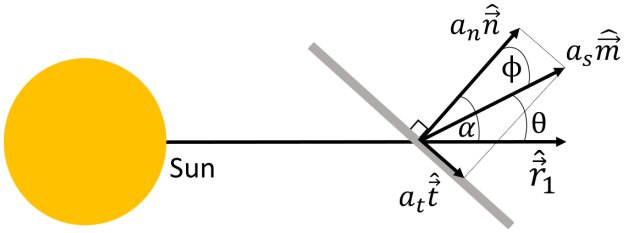

Figure 2 – Non-ideal solar-sail acceleration components adapted from Ref. [20].

of the solar-sail acceleration components can be seen in Fig. 2. The solar-sail pitch angle, α, is defined as the angle between the incoming photons ($\hat{\vec{r}}_1$) and the solar-sail normal direction ($\hat{\vec{n}}$). The solar-sail pitch angle will be limited to $\alpha \in [-70, 70]$ deg as within this range the optical solar-sail model is able to model real sail effects within 1-2% accuracy [21]. An auxiliary angle can be defined as

$$\phi = \arctan\left(\frac{a_t}{a_n}\right) \tag{5}$$

which results in

$$\theta = \alpha - \phi \tag{6}$$

The magnitude of the acceleration components tangent and normal to the solar sail, a_t and a_n, respectively, can be expressed as [8]

$$\begin{cases} a_n = \frac{1}{2}\beta\frac{1-\mu}{r_1^2}\left[(1+\tilde{r}s)\cos^2\alpha + B_f(1-s)\tilde{r}\cos\alpha + (1-\tilde{r})\frac{\varepsilon_f B_f - \varepsilon_b B_b}{\varepsilon_f + \varepsilon_b}\cos\alpha\right] \\ a_t = \frac{1}{2}\beta\frac{1-\mu}{r_1^2}(1-\tilde{r}s)\cos\alpha\sin\alpha \end{cases} \tag{7}$$

where β is the solar-sail lightness number, which is the defined as the ratio between the solar radiation pressure and the solar gravitational acceleration, $\tilde{r}$ is the reflectivity coefficient, s is the coefficient of specular reflection, B_f and B_b are the non-Lambertian coefficients of the front and back side of the solar sail, respectively, and ε_f and ε_b are the front and back side emissivity coefficients, respectively. Note that the dynamical model presented in Section 2.1 is given in the synodic reference frame

$C(x,y)$, which means that the solar-sail acceleration should also be expressed in this frame. An explicit expression for the solar-sail orientation in the $C(x,y)$ frame is retrieved from Ref. [22][1]:

$$\begin{aligned} m_x &= \frac{x-\mu}{r_1}\cos\theta + \frac{y}{r_3}\sin\theta \\ m_y &= \frac{y}{r_1}\cos\theta - \frac{x-\mu}{r_3}\sin\theta \end{aligned} \tag{8}$$

where $r_3 = \sqrt{(x-\mu)^2+y^2}$. Then, the solar-sail acceleration in frame $C(x,y)$ is defined as $\vec{a}_s = \begin{bmatrix} a_s m_x & a_s m_y \end{bmatrix}^T$.

In this study, a lightness number of $\beta = 0.05$ is considered, which is in accordance with expected near-term technological advances [23]. The values and uncertainties of the coefficients for the ideal and optical solar-sail model are presented in Table 1 and are retrieved from NASA's NEA Scout mission [24]. In addition, when the coefficient set of the ideal solar-sail model is substituted in Eq. (7), only a solar-sail acceleration component normal to the sail remains ($a_t = 0$). Consequently, the direction of the total solar-sail acceleration is the same as the direction of the solar-sail normal acceleration ($\vec{m} = \vec{n}$ and therefore $\theta = \alpha$).

Table 1 – The coefficient set and its uncertainty retrieved from Ref. [24] for both an ideal and optical solar-sail model.

	Coefficient	$\tilde{r}$, -	s, -	B_f, -	B_b, -	e_f, -	e_b, -
Ideal	Value	1.0	1.0	-	-	-	-
	Uncertainty	-	-	-	-	-	-
Optical	Value	0.91	0.94	0.79	0.67	0.025	0.27
	Uncertainty	0.005	0.04	0.05	0.05	0.005	0.005

2.3 Coronal Mass Ejection model

The CME-model that describes the propagation of a CME headed towards Earth is retrieved from Ref. [18] and is presented in Fig. 3. It takes into account all key evolutionary aspects and the magnetic field configuration. The key evolutionary aspects are deflection, rotation, expansion, pancaking, front flattening, and rotational skew. The first three aspects relate to the changes in orientation of a CME in interplanetary space, caused mostly by the solar wind. Pancaking is the effect of a latitudinal stretch caused by the radial propagation of a CME. Furthermore, front flattening happens when a CME propagates much faster than the speed of the solar wind, which induces a drag force on the CME and thereby flattens the front part. Finally, rotational skew occurs due to the rotation of the Sun. These key evolutionary aspects can generally be expressed by a force balance as [18]

$$\vec{F}_H = \vec{F}_G + \vec{F}_B \tag{9}$$

where $\vec{F}$ denotes a force vector and the subscripts H, G, and B correspond to hydrodynamic streamlining, gravity, and magnetic tension, respectively. The numerical solution describing the axis of the CME (Fig. 10) to the force balance is defined in a polar reference frame ($P(l,\gamma)$) with the origin P at the center of the Sun, l is the radius, and γ is the angular coordinate which is defined to be positive in counterclockwise direction. The numerical solution is equal to [18]

$$l(\gamma) = R_t \cos^n(a\gamma) \tag{10}$$

where $R_t = 1+\mu$ is the toroidal height of the CME, $n = 0.25$ is the coefficient of front flattening, and $a = \frac{\pi}{2\gamma_{hw}}$ where $\gamma_{hw} = 25$ deg is the angular half-width of the axis [18].

[1]The clock angle, used to define the solar-sail orientation in three-dimensional space, is set equal to 90 deg in the two-dimensional formulation used in this paper.

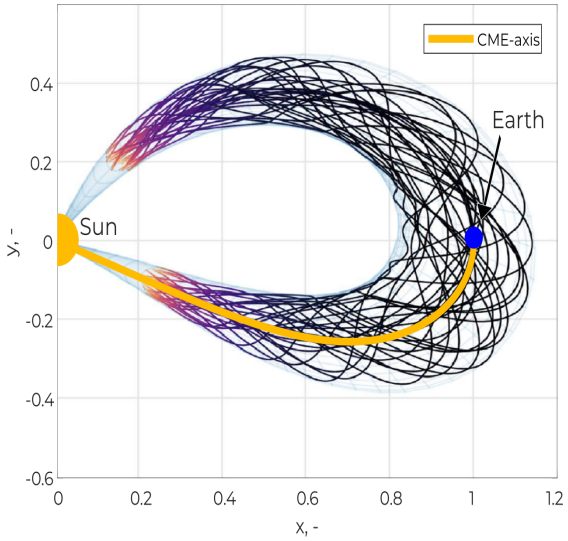

Figure 3 – Coronal Mass Ejection axis (CME-axis) with the CME-model from Ref. [18] projected onto the ecliptic plane in the synodic reference frame $C(x,y)$.

In this study, the CME-model is reduced to the ecliptic projection of the CME-axis and the CME boundary lines. The objective is to travel as far as possible upstream of the CME-axis, while remaining within the CME boundary lines. The inner and outer boundary lines are modelled with Eq. (10) using $[R_t, n, \gamma_{hw}]$ = $[0.815, 0.18, 15]$ and $[1.115, 0.20, 32]$, respectively [18]. As a result, the radial size of the CME when crossing the x-axis is 0.33 AU, which is equal to the mean radial size of all detected CMEs during solar cycle 23 (1996 - 2009) [25]. Note that only the "bottom part" (i.e., the fourth quadrant of the (x,y)-plane) of the CME is taken into consideration, as shown by the CME-axis in Fig. 3. Because of the dynamics of the Sun and the Earth, incoming CMEs propagate in an anti-clockwise direction. As a result, upstream CME detection is restricted to the fourth quadrant of the (x,y)-plane.

3. Optimal Control Problem

The increase in warning time with respect to current missions at the Sun-Earth L_1 point, k, at a particular point, p, see Fig. 4, is obtained by finding the perpendicular projection of p onto the CME-axis and dividing the arc-length of the CME-axis from that point to the Earth, d_p, by the distance between the L_1 point and the Earth, UD, as

$$k = \frac{d_p}{UD} \tag{11}$$

To optimise the solar-sail trajectory for the increase in warning time with respect to current missions at the Sun-Earth L_1 point, an optimal control problem is defined. In general, an optimal control problem can be defined as finding the state history $\vec{x}(t) = \mathbb{R}^{n_x}$ and the control history $\vec{u}(t) = \mathbb{R}^{n_u}$ where $t \in [t_0, t_f]$ that minimises the cost function J. A direct pseudospectral method will be used to solve the optimal control problem [19]. This method discretises the continuous time interval into a finite number of collocation points (Legendre-Gauss-Lobatto (LGL) nodes) and uses Legendre polynomials to approximate the state and control profiles.

3.1 Methodology

For the problem at hand, J is defined as

$$\begin{aligned} J &= -w_1 \cdot k_{\text{avg}} + w_2 \cdot d_{\text{avg}} - w_3 \cdot k_{\text{max}} \\ &= -w_1 \sum_{p=2}^{N} k_{\text{p}} \frac{(t_p - t_{p-1})}{t_N} + w_2 \sum_{p=2}^{N} ||\vec{r}_p - \vec{r}_{\text{CME,nearest}}|| \frac{(t_p - t_{p-1})}{t_N} - w_3 \cdot \max(k_{\text{p}}) \end{aligned} \tag{12}$$

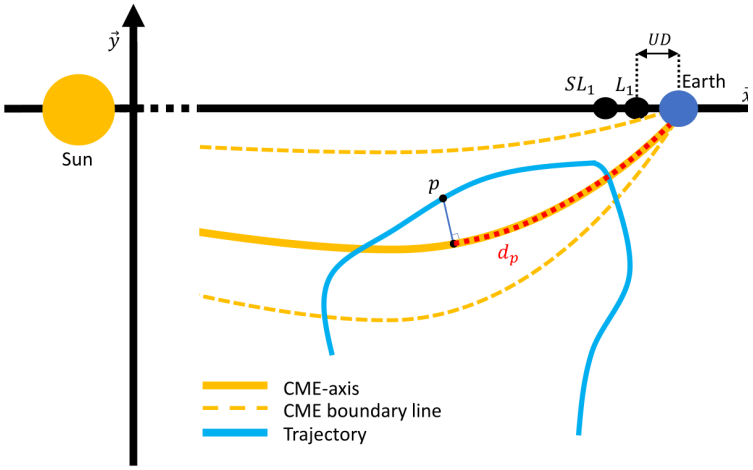

Figure 4 – Definition of the increase in warning time with respect to current missions that are at the Sun-Earth L_1 point.

where w_1, w_2, and w_3 are weights that can be varied to indicate relative importance, p is the considered collocation node, N is the total number of LGL nodes, and the subscript "CME,nearest" denotes the perpendicular projection of p on the CME-axis. Furthermore, it can be seen that J consists of three components: the first term aims at maximising the *average* increase in warning time, the second term aims to minimise the *average* distance to the CME-axis (defined in Fig. 3), and the third term aims to maximise the *maximum* increase in warning time. The minimisation of the average distance to the CME-axis is implemented as it maximises the probability of CME detection. As the shape of the CME from the model laid out in Section 2.3 is based on an average of all detected CMEs in solar cycle 23 (1996 - 2009) [25], a trajectory that lies completely within the depicted CME boundary lines does not guarantee detection of all CMEs heading towards Earth. The total probability that a spacecraft in a particular trajectory detects a CME, P_{total}, can be calculated as

$$P_{\text{total}} = \sum_{\text{RS=min(RS)}}^{\text{RS=max(RS)}} P_{RS} \cdot \frac{f_{RS}}{f} \tag{13}$$

where min(RS) and max(RS) are the minimum and maximum radial sizes of the detected CMEs, respectively, f_{RS} is the number of detected CMEs with radial size RS, and f is the total number of detected CMEs. Note that all data is based on solar cycle 23 and is retrieved from Ref. [25]. Finally, note that the cost function is scaled by time (the term $\frac{t_p - t_{p-1}}{t_N}$) as the LGL nodes are not equally spaced in time [19].

The spacecraft state is composed of the position and velocity state of the spacecraft in the Sun-Earth synodic reference frame, $C(x,y)$, as

$$\vec{x}(t) = [x(t) \quad y(t) \quad v_x(t) \quad v_y(t)]^T \tag{14}$$

with the following bounds

$$[0 \quad -1 \quad -0.5 \quad -0.5]^T \leq \vec{x}(t) \leq [1.15 \quad 0 \quad 0.5 \quad 0.5]^T \tag{15}$$

These bounds have been set such that the spacecraft is able to move in the fourth quadrant of the (x,y)-plane, as was illustrated in Section 2.3. The control variable is the solar-sail pitch angle profile with the corresponding bounds

$$-70 \text{ deg} \leq u(t) = \alpha(t) \leq 70 \text{ deg} \tag{16}$$

The bounds on the time are set as

$$t_0 = 0, \qquad 10 \leq t_f \leq 50 \tag{17}$$

which corresponds to $1.59\text{y} \leq t_f \leq 7.96\text{y}$ in dimensional time units. The values have been chosen based on the period of the initial-guess trajectories which are in the order of 3.5 years (see Section 3.2).

To guarantee periodicity, the state and control at the initial and final time are set equal to each other as

$$\vec{x}(t_0) = \vec{x}(t_f) \qquad \vec{u}(t_0) = \vec{u}(t_f) \tag{18}$$

Note that the evaluation of the cost function in Eq. (12) starts at $p = 2$, because $p = 1$ and $p = N$ are effectively the same as a result of the constraints in Eq. (18).

A path constraint is imposed on the problem to ensure that the spacecraft always remains within the CME zone. It is defined as

$$y_{\text{CME,boundary,L}}(x_p) \leq y_p \leq y_{\text{CME,boundary,U}}(x_p) \tag{19}$$

where $y_{\text{CME,boundary,L}}(x_p)$ and $y_{\text{CME,boundary,U}}(x_p)$ are the lower and upper y-coordinate of the CME boundary, respectively, which are modelled as an eighth order polynomial. As a result of this constraint, the required number of spacecraft to maintain a constellation of continuous CME monitoring is one. This constraint is implemented to be able to properly compare the performance of the different optimised solutions (due to various relative weight specifications in Eq. 12) as a discrepancy in the required number of spacecraft would yield the comparison inconsistent and unusable.

The optimisation solution ensures that *only* at the nodes the state and control abide by the dynamics, the imposed constraints, and the bounds. In order to check whether the entire trajectory adheres to them, the trajectory is re-integrated in MATLAB®. The re-integration takes the initial conditions from the optimisation solution and integrates the state until the final time. The control, i.e., the solar-sail pitch angle, is retrieved by interpolating the optimisation solution using shape-preserving piecewise cubic interpolation [26]. The difference in state at $t = t_f$ between the re-integrated solution and the final node of the optimisation solution is an indication of the validity of the optimisation solution, i.e., the constraints are adhered to across the full trajectory and not only at the nodes. Error values on the position and velocity at the end of the re-integrated trajectory of $\Delta r \leq 10^{-3}$ and $\Delta v \leq 10^{-2}$ are taken as a reference to regard a trajectory as valid [27].

The direct pseudospectral method from the C++ open-source package PSOPT is used to solve the optimal control problem [19]. This algorithm has proven to be a successful method to solve optimal control problems in, among others, solar-sail trajectory optimisation problems [28]. Furthermore, PSOPT requires an initial guess to start the optimisation, which will be given in the next section.

3.2 Initial-guess trajectories

Initial guesses for the optimal control problem are found by generating heteroclinic connections between AEPs in the vicinity of the SL_1 and SL_5 points. The heteroclinic connections consist of a linkage between the unstable manifold of an AEP close to the SL_1 point and the stable manifold of an AEP close to the SL_5 point and vice versa to make the trajectory periodic [29]. Along the manifolds, a constant sail pitch angle is assumed. A genetic algorithm is employed to find the optimal AEPs and optimal piece-wise constant sail pitch angle along each manifold segment. Here, optimal refers to either the maximum increase in warning time or average increase in warning time. More details on the methodology can be found in Ref. [30]. Note that these initial-guess trajectories are sub-optimal due to the piece-wise constant solar-sail pitch angles and the fact that minor discontinuities in the state exist at the linkages of the unstable and stable manifolds. These sub-optimalities are overcome by PSOPT.

3.3 Results

Note that, in this section, the following assumptions are adopted:

- An ideal solar-sail model is used.
- A lightness number of $\beta = 0.05$ is utilised.

The weights w_1, w_2, and w_3 in the cost function that are defined in Eq. (12) can be varied to change the relative importance of the metrics defined. In an effort to eliminate the subjectivity in choosing a set of weights, a large number of combinations of sets of weights are evaluated. Consequently, an inventory of the capabilities of using a solar sail for solar-storm detection is obtained.

3.3.1 Inventory

In total, approximately 600 combinations have been evaluated with weights in the ranges $w_1 = [0,1]$, $w_2 = [0,4000]$, and $w_3 = [0,1]$. These ranges have been chosen such that each component in the cost function can be emphasised with equal (relative) importance. A continuation method is employed and is executed in a sequential order where two weights are kept fixed and one is varied gradually. For example, the solution to the optimisation problem with weights $[w_1, w_2, w_3] = [1, 2000, 0.5]$ is used as an initial guess for the optimisation problem with weights $[w_1, w_2, w_3] = [1, 2000, 0.55]$.

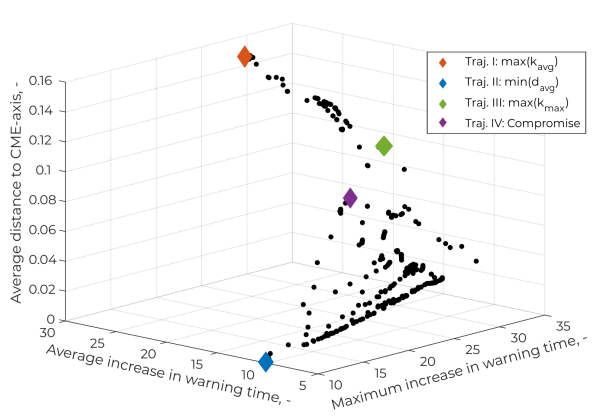

(a) Isometric view.

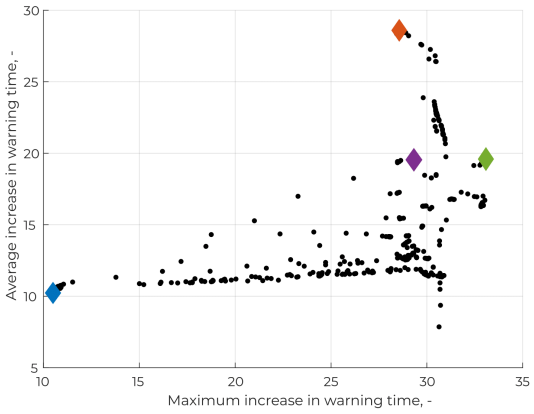

(b) Side view displaying the correlation between the maximum and average increase in warning time.

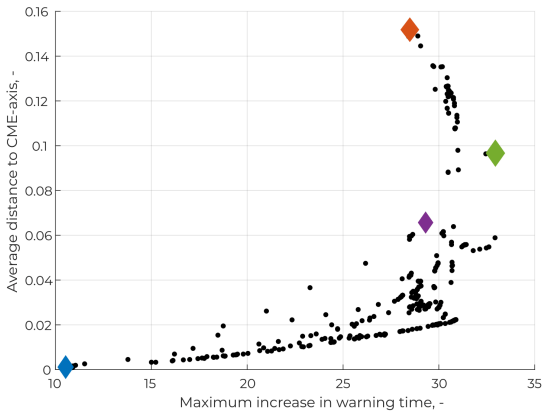

(c) Side view displaying the correlation between the maximum increase in warning time and the average distance to the CME-axis.

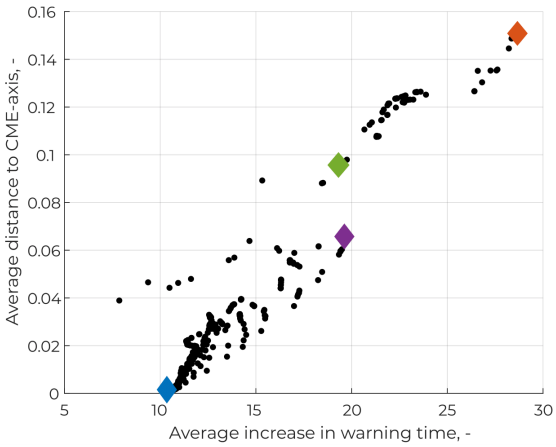

(d) Side view displaying the correlation between the average increase in warning time and the average distance to the CME-axis.

Figure 5 – PSOPT: Inventory of the properties of converged solar-sail trajectories using a number of nodes $N = 25$.

In PSOPT, the maximum number of iterations is set to 3000, the convergence tolerance to 10^{-4}, and the number of LGL nodes to $N = 25$ to limit the computational effort. The inventory of the converged solutions is presented in Fig. 5. Four trajectories are indicated that have the following properties:

- Trajectory I maximises the average increase in warning time: max(k_{avg}).

- Trajectory II maximises the probability of CME detection by minimising the average distance to the CME-axis: min(d_{avg}).
- Trajectory III maximises the maximum increase in warning time: max(k_{max}).
- Trajectory IV is a compromise between the three aspects (k_{avg}, d_{avg}, and k_{max}).

Several observations can be made in the solar-sail inventory. For an average and maximum increase in warning time of a factor 10, the average distance to the CME-axis is zero and therefore the probability of CME detection is 100% (see the blue marker in Fig. 5). Furthermore, a maximum increase in warning time of a factor of approximately 31 can be achieved while both the average increase in warning time and the average distance to the CME-axis remain small as indicated by the black dots in the bottom right of Fig. 5b and Fig. 5c. Increasing the average increase in warning time does however impact the average distance to the CME-axis; these two objectives demonstrate a linear relationship as presented in Fig. 5d. This trend is caused by the fact that while the spacecraft travels further upstream of the CME-axis, it moves away from the CME-axis. This observation can be illustrated by taking a detailed look at trajectories I and II (indicated by the red and blue marker) from Fig. 5, obtained with weights $[w_1, w_2, w_3] = [1, 0, 0]$ and $[1, 4000, 0]$, respectively. The positional state and control profiles are displayed in Fig. 6 and their properties are presented in Table 2. As illustrated by trajectory II, solely maximising the average increase in warning time results in a trajectory that is (almost) stationary in close proximity of an AEP [29] which is furthest upstream of the CME-axis, while still remaining within the CME detection zone. This trajectory achieves a maximum and average increase in warning time of a factor 28.5 with a probability of CME detection of 48.7%. On the contrary, solely maximising the probability of CME detection results in a trajectory that remains (almost) stationary in close proximity of an AEP on the CME-axis and achieves a maximum and average increase in warning time of a factor 10.5 and a probability of CME detection of 100.0%. Note that the magnitude of the solar-sail pitch angle, i.e., the control effort, is small as displayed in Fig. 6b.

Table 2 – PSOPT: properties of trajectories I-IV that are displayed in Fig. 6 and Fig. 7.

Trajectory	k_{avg}, -	P_{total}, %	k_{max}, -	T, yr	N, -
I: max(k_{avg})	28.48	48.73	28.51	1.60	25
II: min(d_{avg})	10.51	100.0	10.53	4.64	25
III: max(k_{max})	24.22	72.22	29.46	2.76	65
IV: Compromise	19.09	89.12	29.17	4.69	85

The two trajectories displayed in Fig. 6 have a re-integration error well below $\Delta r \leq 10^{-3}$ and $\Delta v \leq 10^{-2}$ such that the trajectories can be regarded as feasible. However, the re-integration errors of the trajectories that are associated with max(k_{max}) and a compromise between the three elements, trajectory III and IV ($[w_1, w_2, w_3] = [1, 125, 0.125]$ and $[1, 250, 0.15]$, respectively, in Eq. (12)), as indicated in Fig. 5 are both in the order of 0.4 and are therefore not valid [27]. An explanation for these relatively large re-integration errors can be explained by the number of nodes that is used in the optimisation. For a small number of nodes, $N = 25$ in this case, the solar-sail pitch angle interpolation becomes less accurate as there are larger time steps in-between data points, resulting in an overall less accurate re-integration. Consequently, before any conclusions can be drawn from trajectory III and IV, the optimisation solutions should be refined, i.e., more nodes should be added, which might result in valid and therefore realistic trajectories.

3.3.2 Mesh-refinement

PSOPT has a built-in functionality to gradually add more nodes to the optimisation problem, using the solution of the previous evaluation as an initial guess [19]. This mesh-refinement process is executed on trajectories III and IV until the validity requirement is met. It is observed that trajectory III complies with this requirement, both in position and velocity, at $N = 65$, and that trajectory IV satisfies the requirement at $N = 85$. The mesh-refined trajectories III and IV are displayed in Fig. 7 and their properties are displayed in Table 2.

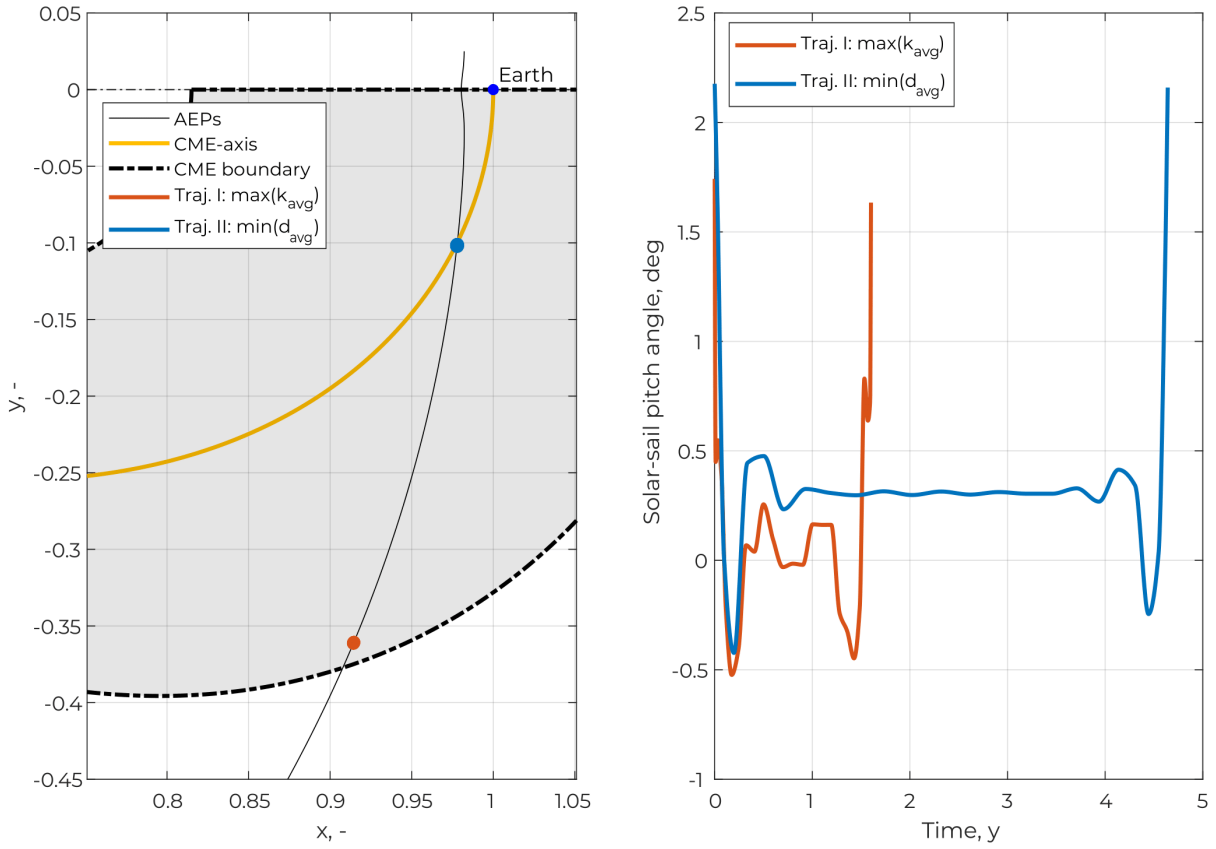

(a) Positional state.

(b) Control profile.

Figure 6 – PSOPT: trajectory I (max(k_{avg})) and II (min(d_{avg})) within the solar-sail inventory using a number of nodes of $N = 25$.

The value for the maximum increase in warning time is approximately the same for the two trajectories, equal to ≈ 29.5. In addition, this value closely corresponds to the value for the maximum increase in warning time obtained for trajectory I. It gives the impression that such a value can easily be obtained. It can be concluded that the optimisation is more a trade-off between the average increase in warning time and the probability of CME detection, displayed by a value of the average increase in warning time and the probability of CME detection of [24.2, 72.2%] and [19.1, 89.1%] for trajectories III and IV, respectively. This inverse trend was also observed in trajectories I, II, and the inventory in Fig. 5.

The optimised and mesh-refined solutions for trajectory III and IV show a multi-revolutionary trajectory. One revolution of this trajectory has the goal to travel furthest upstream of the CME-axis. This revolution is almost identical for the two trajectories (Fig. 7a) and is characterised by the maximum value in solar-sail pitch angle of approximately -15 deg. The other revolutions are a result of a trade-off between the average increase in warning time and the average distance to the CME-axis; if a revolution is closer to the CME-axis, both the average increase in warning time and the average distance to the CME-axis are smaller than when this revolution reaches further upstream. Lastly, note that it is assumed that the solar sail has no constraint on the rate of change of the pitch angle, while in reality there is a practical limitation. The results show a maximum value of this rate of change in trajectory IV of 0.33 degrees per *day*. Compared to a practical limitation of the rate of change of 144 degrees per *hour*, the trajectories still satisfy this operational constraint [31].

3.3.3 Overview

An overview of the properties of the four trajectories that were outlined in the previous sections is given in Table 2. In addition, the increase in warning time and distance to the CME-axis as a

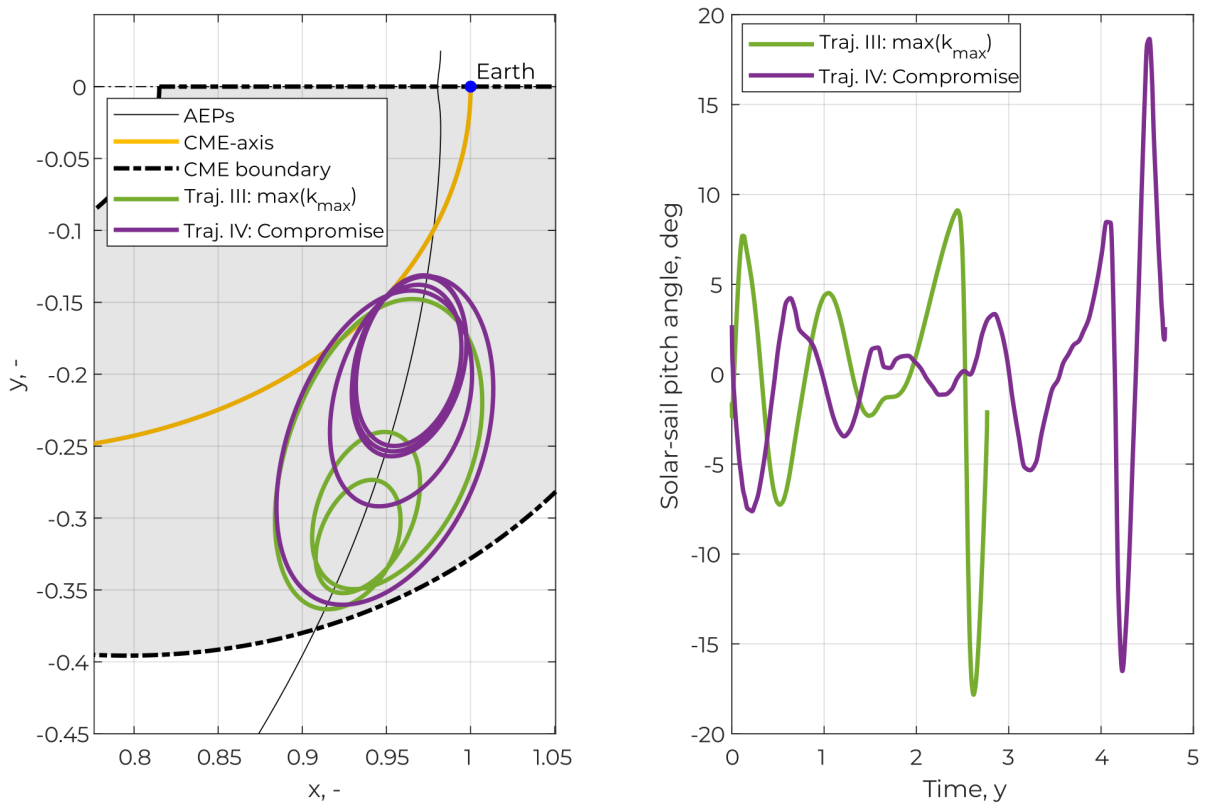

(a) Positional state.

(b) Control profile.

Figure 7 – PSOPT: the mesh-refined trajectories III (max($k_{\max}$)) and IV (compromise) within the solar-sail inventory using a number of nodes of $N = 65$ and $N = 85$, respectively.

function of the orbital period for trajectories I-IV are presented in Fig. 8. Note that other points in the inventory (Fig. 5) can be selected to obtain a trajectory with different desired properties. For instance, while still reaching the maximum increase in warning time, the balance between the average increase in warning time and the probability of CME detection, can be shifted to satisfy a particular requirement/preference.

The displayed periodic solar-sail trajectories exhibit an (average and maximum) increase in solar-storm warning time in the range of a factor 20 to 30 with respect to current missions at L_1. This results in an absolute warning time of approximately 10 to 30 hours. It is well short of the requirement of two to three days to fully prepare for disruption outlined in Ref. [6]. However, electronic systems on Earth are upgraded to be better protected against the impact of solar storms, e.g., by having more safety mechanisms in place, and there is increasing awareness of the impact of solar storms in society [32]. It is therefore expected that the preparation time will decrease over the years due to better mitigation plans. In addition, other methods such as a spacecraft at L_5 that allows for earlier *predictions* of solar storms should be considered: a spacecraft from the viewpoint of L_5 is able to look at the surface of the Sun that rotates towards Earth four to five days later [1]. Still, a spacecraft that enables for earlier *detection* is essential in preparing society for an event as it takes away the (great) uncertainty of the magnitude and propagation path of a solar storm [1, 6]. A combination of a spacecraft at L_5 and a solar-sail spacecraft in a periodic solar-sail trajectory outlined in this section may therefore be the solution to receive a timely warning of an approaching solar storm.

3.4 Sensitivity analysis

The trajectories displayed in Section 3.3 employed an ideal solar-sail model. The performance impact due to the implementation of the optical solar-sail model, which is laid out in Section 2.2, is presented in Table 3. The trajectories computed using an optical sail model are denoted by the

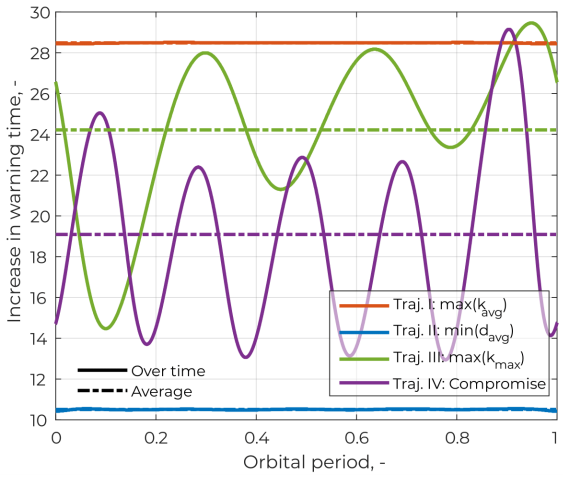

Figure 8 – PSOPT: the increase in warning time as a function of the orbital period for trajectories I-IV.

subscript "opt". It is observed that the difference with respect to an ideal solar-sail model remains small. The relatively larger differences for trajectory II_{opt} may be associated with the fact that this practically stationary trajectory is closest to the Earth: the optical sail model results in a smaller acceleration, hence the AEP shifts closer to the Earth [29]. In addition, closer to the Earth, the gradient of the CME-axis is steeper (Fig. 10), which means that the practically stationary trajectory closer to the Earth experiences a larger performance impact than trajectories farther away from the Earth. The overall small performance difference can be attributed to the small solar-sail pitch angle ($\alpha \in [-20 \text{ deg}, 20 \text{ deg}]$) for all trajectories. As a result, the solar-sail acceleration component tangent to the sail (Eq. (7)) remains small meaning that the difference between the ideal and optical solar-sail model is kept to a minimum [8]. Finally, it was observed that the *uncertainty* in the coefficient set of the optical solar-sail model (Table 1) does not have a considerable effect on the performance of the trajectories: the properties are only marginally affected by 0.5-2.0%, approximately in the same order as the performance impact due to the implementation of the optical sail model.

Table 3 – PSOPT: properties of trajectories I-IV evaluated using an optical solar-sail model and the difference with respect to the ideal solar-sail model, Δ_{id}.

Trajectory	k_{avg}, -	Δ_{id} (%)	P_{total}, -	Δ_{id} (%)	k_{max}, -	Δ_{id} (%)
I_{opt}: max(k_{avg})	28.36	0.42	48.62	0.22	28.39	0.42
II_{opt}: min(d_{avg})	10.12	3.71	99.94	0.06	10.14	3.70
III_{opt}: max(k_{max})	24.11	0.45	72.12	0.14	29.31	0.51
IV_{opt}: Compromise	19.02	0.37	88.66	0.51	29.00	0.58

All of the trajectories displayed in this paper utilised a lightness number of $\beta = 0.05$ which is in accordance with mid-term technological advances [23]. However, it is interesting to assess the performance of solar sails in the far-term future, which are predicted to have a lightness number of 0.1 [33]. In addition, current state-of-the-art allow for a lightness number of 0.01 [34]. A continuation method (the same strategy as explained in the previous section) on the lightness number has been performed on trajectories I_{opt} - IV_{opt} for $\beta \in [0.01, 0.1]$. The results show that for an increase in lightness number of $\Delta\beta = 0.01$, the trajectory properties will increase by 1%, and vice versa. Therefore, the performance of the trajectories displayed in this paper is expected to increase with improving solar-sail technology.

4. Conclusion

In this paper, solar-sail periodic trajectories in the vicinity of the Sun-Earth SL_1 and SL_5 points have been investigated to increase the solar-storm warning time with respect to current missions

at the Sun-Earth L_1 point. These periodic trajectories trade-off three objectives: maximising the maximum and average increase in warning time as well as minimising the average distance to the CME-axis, which in turn maximises the probability that a CME is detected. In this study, an ideal solar-sail model and a lightness number of $\beta = 0.05$ have been used to compute trajectories. Four trajectories have been obtained by specifying the relative importance between the three objectives. Trajectory I maximises the average increase in warning time, equal to approximately a factor 28.5, which results in a spacecraft practically stationary in close proximity of an AEP furthest upstream of the CME-axis. Because of its location, the spacecraft has a probability of 49% that it detects a CME. Alternatively, trajectory II minimises the average distance to the CME-axis which results in a spacecraft practically stationary in close proximity of this axis, thereby having a 100% probability of CME detection, and has an average (and maximum) increase in warning time of approximately a factor 10.5. Trajectory III was initially selected to maximise the maximum increase in warning time, which was equal to a factor 29.5. However, it was observed that this maximum increase in warning time could easily be achieved for a range of values for the other two objectives, allowing to find a trajectory that satisfies a particular requirement or preference. Trajectory III is thus a somewhat random compromise between the three objectives. The same holds for trajectory IV. Trajectory III and IV have an average increase in warning time and probability of CME detection of approximately [24.2, 72%] and [19.1, 89%], respectively. In general, a larger increase in average warning time results in a smaller probability that a CME is detected (for a maximum increase in warning time of approximately a factor 29.5). Finally, a sensitivity analysis has been conducted to assess the effect of the solar-sail model and the lightness number. Compared to the ideal solar-sail model, an optical solar-sail model yields a modest decrease in performance of up to 3.7%. An increase in lightness number of 0.01 yields a performance increase of approximately 1% . These magnitudes can change depending on the nature of the trajectory. In general, when the trajectory is relatively close to the Earth the performance is more sensitive to a change in lightness number than trajectories further away.

5. Contact Author Email Address

For questions, comments, and general contact, the authors can be reached at niels.bakx@live.nl.

6. Copyright Statement

References

[1] Milan, S., Dunlop, M., Fazakerley, A., Hubert, B., Lavraud, B., Østgaard, N., Shi, J., Escoubet, C., Taylor, M., Falkner, P., and Wielders, A.. "Kuafu: Exploring the sun-earth connection," *Astronomy and Geophysics*. vol. 53. no. 4. pp. 4.21 – 4.24. 2012.

[2] Vulpetti, G., Johnson, L., and Matloff, G.. *Solar sails: A novel approach to interplanetary travel*. 2015.

[3] Eastwood, J., Hapgood, M., Biffis, E., Benedetti, D., Bisi, M., Green, L., Bentley, R., and Burnett, C.. "Quantifying the economic value of space weather forecasting for power grids: An exploratory study," *Space Weather*. 2018.

[4] Homeier, N. and Wei, L.. "Solar storm risk to the north american electric grid," tech. rep.. Atmospheric and Environmental Research (AER). 2013.

[5] Riley, P.. "On the probability of occurrence of extreme space weather events," *Space Weather*. vol. 10. no. 2. 2012.

[6] Gibney, E.. "Europe lines up for solar-storm view," *Nature*. vol. 541. p. 271. 2017.

[7] Heiligers, J., Diedrich, B., Derbes, B., and McInnes, C.. "Sunjammer: Preliminary end-to-end-mission design," in *AIAA/AAS Astrodynamics Specialist Conference 2014*. p. 4127. American Institute of Aeronautics and Astronautics. 2014.

[8] McInnes, C.. *Solar sailing: Technology, Dynamics and Mission Applications*. Berlin: Springer-Praxis Books in Astronautical Engineering, Springer-Verlag. 1999.

[9] Martínez, G.. "Solar-sail surfing along invariant manifolds to increase the warning time for solar storms," Master's thesis. 2020. Delft University of Technology.

[10] Tsuda, Y., Mori, O., Funase, R., Sawada, H., Yamamoto, T., Saiki, T., Endo, T., Yonekura, K., Hoshino, H., and Kawaguchi, J.. "Achievement of ikaros-japanese deep space solar sail demonstration mission," in *Acta Astronautica*. 2013.

[11] Johnson, L., Whorton, M., Heaton, A., Pinson, R., Laue, G., and Adams, C.. "Nanosail-d: A solar sail demonstration mission," in *Acta Astronautica*. 2011.

[12] Betts, B., Spencer, D., Bellardo, J., Nye, B., Diaz, A., Plante, B., Mansell, J., Fernandez, M., Gillespie, C., and Garber, D.. "Lightsail 2: Controlled solar sail propulsion using a cubesat," in *Proceedings of the International Astronautical Congress, IAC*. 2019.

[13] McNutt, L., Johnson, L., Clardy, D., Castillo-Rogez, J., Frick, A., and Jones, L.. "Near-earth asteroid (nea) scout," in *AIAA SPACE 2014 Conference and Exposition*. 2014.

[14] Wilkie, W., Fernandez, J., Stohlman, O., Schneider, N., Dean, G., Kang, J., Warren, J., Cook, S., Brown, P., Denkins, T., Horner, S., Tapio, E., Straubel, M., Richter, M., and Heiligers, J.. "An overview of the nasa advanced composite solar sail (acs3) technology demonstration project," *AIAA SciTech 2021 Forum*. Virtual Event.

[15] Mori, O., Matsumoto, J., Chujo, T., Matsushita, M., Kato, H., Saiki, T., Tsuda, Y., Kawaguchi, J., Terui, F., Mimasu, Y., Ono, G., Ogawa, N., Takao, Y., Kubo, Y., Ohashi, K., Sugihara, A., Okada, T., Iwata, T., and Yano, H.. "Solar power sail mission of okeanos," *Astrodynamics*. vol. 4. pp. 233 – 248. 2020.

[16] Heiligers, J. and McInnes, C.. "Novel solar sail mission concepts for space weather forecasting," vol. 152. 01 2014.

[17] Barnhart, D., Vladimirova, T., and Sweeting, M.. "Very-small-satellite design for distributed space missions," *Journal of Spacecraft and Rockets*. vol. 44. no. 6. pp. 1294 – 1306. 2007.

[18] Isavnin, A.. "FRiED: A NOVEL THREE-DIMENSIONAL MODEL OF CORONAL MASS EJECTIONS," *The Astrophysical Journal*. vol. 833. no. 2. pp. 267 – 276. 2016.

[19] Becerra, V.. "Solving complex optimal control problems at no cost with psopt," *Proceedings of the IEEE International Symposium on Computer-Aided Control System Design*. pp. 1391–1396. 2010.

[20] Heiligers, J., Fernandez, J., Stohlman, O., and Wilkie, K.. "Trajectory design for a solar-sail mission to asteroid 2016 ho3," *Astrodynamics*. vol. 3. no. 3. pp. 231–246. 2019.

[21] Spencer, H. and Carroll, K.. *Real solar sails are not ideal, and Yes It Matters*. pp. 921–940. Berlin, Heidelberg: Springer Berlin Heidelberg. 2014.

[22] McInnes, A.. "Strategies for solar sail mission design in the circular restricted three-body problem," Master's thesis. August 2000. Purdue University.

[23] Dachwald, B., Mengali, G., Quarta, A., and Macdonald, M.. "Parametric model and optimal control of solar sails with optical degradation," *Journal of Guidance, Control and Dynamics*. vol. 29. no. 5. pp. 1170–1178. 2006.

[24] Heaton, A., Ahmad, N., and Miller, K.. "Near earth asteroid scout thrust and torque model," 2017.

[25] Richardson, I. and Cane, H.. "Near-earth interplanetary coronal mass ejections during solar cycle 23 (1996 - 2009): Catalog and summary of properties," *Solar Physics*. vol. 264. pp. 189–237. June 2010.

[26] "Matlab 1-d data interpolation," 2021. Date Accessed: 11-10-2021. https://nl.mathworks.com/help/matlab/ref/interp1.html.

[27] Vergaaij, M. and Heiligers, J.. "Time-optimal solar sail heteroclinic-like connections for an earth-mars cycler," *Acta Astronautica*. vol. 152. pp. 474–485. 2018.

[28] "Psopt - publications," 2021. Date Accessed: 10-10-2021. https://www.psopt.net/publications.

[29] Farrés, A. and Jorba, A.. "Solar sailing with invariant manifolds in the earth-sun system," *Proceedings of the International Astronautical Congress, IAC*. vol. 7. no. April. pp. 5323–5333. 2015.

[30] Bakx, N.. "Using solar-sail induced dynamics to increase the warning time for solar storms heading towards earth," Master's thesis. 2021. Delft University of Technology.

[31] Wilkie, W. Personal Communication. May 2021. NASA Langley Research Center.

[32] Wendel, J.. "Protecting earth from solar storms," *Eos*. vol. 96. May 2015.

[33] Young, R.. "Updated heliostorm warning mission: Enhancements based on new technology," 04 2007.

[34] Spencer, D., Johnson, L., and Long, A.. "Solar sailing technology challenges," *Aerospace Science and Technology*. vol. 93. p. 105276. 2019.